COMMUNICATION

ADVANCED
MATERIALS

www.advmat.d

Check for
updates

In Situ Topotactic Transformation of an Interstitial Alloy for CO Electroreduction

Changming Zhao, Gan Luo, Xiaokang Liu, Wei Zhang, Zhijun Li, Qian Xu, Qinghua Zhang, Huijuan Wang, Deming Li, Fangyao Zhou, Yunteng Qu, Xiao Han, Zezhou Zhu, Geng Wu, Jing Wang, Junfa Zhu, Tao Yao,* Yafei Li,* Henny J.M. Bouwmeester, and Yuen Wu*

Electrochemical reduction of CO to value-added products holds promise for storage of energy from renewable sources. Copper can convert CO into multi-carbon (C$_{2+}$) products during CO electroreduction. However, developing a Cu electrocatalyst with a high selectivity for CO reduction and desirable production rates for C$_{2+}$ products remains challenging. Herein, highly lattice-disordered Cu$_3$N with abundant twin structures as a precursor electrocatalyst is examined for CO reduction. Through in situ activation during the CO reduction reaction (CORR) and concomitant release of nitrogen, the obtained metallic Cu° catalyst particles inherit the lattice dislocations present in the parent Cu$_3$N lattice. The de-nitrified catalyst delivers an unprecedented C$_{2+}$ Faradaic efficiency of over 90% at a current density of 727 mA cm^{-2} in a flow cell system. Using a membrane electrode assembly (MEA) electrolyzer with a solid-state electrolyte (SSE), a 17.4 vol% ethylene stream and liquid streams with concentration of 1.45 M and 230 × 10^{-3} M C$_{2+}$ products at the outlet of the cathode and SSE-containment layer are obtained.

Electrosynthesis of C$_{2+}$ products from CO is an efficient utilization of low-cost renewable energy sources.[1–3] Compared with traditional chemical processes, which require high temperatures and high pressures, electrochemical reduction of CO shows a high energy efficiency under ambient operating conditions and significantly reduces production costs.[4,5] At present, there are multiple efficient electrocatalysts that can reduce CO$_2$ to CO,[6] unfortunately with a low efficiency of production of C$_{2+}$ products. Recently, it been found that a tandem strategy can enhance the activity and selectivity to C$_{2+}$ products,[7,8] noting that CO is the key reaction intermediate in the CO$_2$ reduction reaction (CO$_2$RR). The inevitable desorption of CO largely limits the activity and selectivity of the direct CO$_2$RR toward C$_{2+}$ products.[1,9]

C. Zhao, D. Li, F. Zhou, Dr. Y. Qu, X. Han, G. Wu, Dr. J. Wang, Prof. Y. Wu
Department of Chemistry
iChEM (Collaborative Innovation Center of Chemistry
for Energy Materials)
University of Science and Technology of China
Hefei 230026, China
E-mail: yuenwu@ustc.edu.cn

Dr. G. Luo, Prof. Y. Li
Jiangsu Collaborative Innovation Centre
of Biomedical Functional Materials
Jiangsu Key Laboratory of New Power Batteries
School of Chemistry and Materials Science
Nanjing Normal University
Nanjing 210023, China
E-mail: liyafei.abc@gmail.com

X. Liu, W. Zhang, Prof. T. Yao
National Synchrotron Radiation Laboratory
University of Science and Technology of China
Hefei 230029, P.R. China
E-mail: yaot@ustc.edu.cn

Dr. Z. Li
Provincial Key Laboratory of Oil and Gas Chemical Technology
College of Chemistry and Chemical Engineering
Northeast Petrolrum University
Daqing 163318, P. R. China

The ORCID identification number(s) for the author(s) of this article can be found under https://doi.org/10.1002/adma.202002382.

Dr. Q. Xu, Prof. J. Zhu
The Catalysis and Surface Science Endstation at the BL11U beamline in the National Synchrotron Radiation Laboratory (NSRL) in Hefei
China

Dr. Q. Zhang
Institute of Physics
Chinese Academy of Sciences
Beijing 100190, P. R. China

H. Wang
USTC Center for Micro and Nanoscale Research and Fabrication
University of Science and Technology of China
P. R. China

Dr. Z. Zhu
Division of Advanced Nanomaterials
Suzhou Institute of Nano-tech and Nano-bionics
Chinese Academy of Sciences
Suzhou 215123, China

Prof. H. J. M. Bouwmeester
Electrochemistry Research group
Membrane Science and Technology
MESA+ Institute for Nanotechnology
University of Twente
P.O. Box 217, Enschede 7500 AE, The Netherlands

Prof. H. J. M. Bouwmeester
CAS Key Laboratory of Materials for Energy Conversion
Department of Materials Science and Engineering
University of Science and Technology of China
Hefei 230026, P. R. China

To date, copper-based materials are known as the best catalysts for conversion of CO_2 and/or CO into C_{2+} products (e.g., ethanol, acetate, ethylene, and propanol).[10] However, conventional Cu electrodes suffer from a low production rate and a poor Faradaic efficiency due to CO_2/CO mass-transport limitations and the competing hydrogen evolution reaction (HER).[11] Over the past decades, researchers have demonstrated that crystal defects, such as grain boundaries,[12] lattice dislocations,[3,13] significantly enhances the activity toward CO/CO_2 reduction. These lattice defects are characterized by the presence of unsaturated coordination sites and may increase the CO binding energy, thereby increasing the concentration of absorbed CO.[3,9] Their presence may further lower the energy barrier for the C—C coupling reaction by stabilizing corresponding *C_2 intermediates such as *OC—COH, *C—CO, and *HC—CO, ultimately improving the activity and selectivity of CO/CO_2RR.[9] However, it remains a big challenge to obtain highly defective and active Cu catalysts.[3] Cu adopts a face-centered cubic (fcc) structure and exhibits no obvious tendency during nucleation and growth to form extended defects such as dislocations, twins and stacking faults.[14,15]

Despite progress in recent years, it remains a challenge to control the crystalline structure of nanocrystals, because of the lack of a quantitative knob to manipulate their nucleation and growth.[15] In this work, we successfully prepared copper nitride (Cu_3N) nanocrystals with abundant twin structures by controlling the growth rate of these crystals. At low growth rates, Cu adatoms migrate across the surface and are assembled in crystal facets with unique symmetry, minimizing the total surface energy.[16] When the growth rate is increased, crystal growth is governed by kinetic control due to the fact that the rate of addition of adatoms exceeds that of diffusion.[17] As a result, defect-rich seeds grow anisotropically and evolve into nanocrystals with a low-symmetry structure. Consequently, the formation of distinctive Cu_3N nanocrystals with abundant twin structures will be subject to kinetic control rather than dominated by thermodynamics. During the following electroactivation process, the Cu_3N precursor catalyst is reduced in situ to metallic $Cu°$. Because of the unique structure of the metal/non-metal interstitial alloy and the slow release of the interstitial nitrogen atoms, the as-obtained $Cu°$ catalyst inherit the lattice dislocations present in parent Cu_3N, thereby rendering it great potential in CORR.

Figure 1a schematically shows the formation process of Cu_3N nanoparticles with a low and high density of (branched) lattice dislocations, henceforth referred to as Cu_3N-LDD and Cu_3N-HDD, respectively, through the use of different growth rates. At increased temperature, Cu_3N polycrystalline seeds with multiple twin defects and stacking faults are formed (Figure S1, Supporting Information). At a given growth rate, the crystal seeds evolve into nanocrystals with distinctive crystallographic facets. The growth rate can be regulated by controlling the flow rate of ammonia in the solution synthesis. Higher growth rates lead to anisotropic shapes of the Cu_3N polycrystals due to the generation of abundant twin structures. Transmission electron microscopy (TEM) and scanning electron microscopy (SEM) images (Figure 1b–d and Figures S2–S5, Supporting Information) show that the average diameter of the Cu_3N-LDD and Cu_3N-HDD nanoparticles is about 150 nm.

Energy-dispersive X-ray spectroscopy (EDS) mapping images confirm that Cu and N are uniformly distributed in both of them (Figure 1e and Figure S3, Supporting Information), which is indicative of homogeneous doping of N in the host materials. The Cu_3N-LDD nanoparticles are polycrystalline as confirmed by high-angle annular dark-field scanning transmission electron microscopy (HAADF-STEM) (Figure S3, Supporting Information). The HAADF-STEM images of the nanosheets on Cu_3N-LDD (Figure 1f,g) confirm that these are twinned with a misorientation angle of 37°. Another HAADF-STEM image obtained with a different incident angle of the electron beam is given in Figure S6, Supporting Information. The valence state and composition evolution of Cu_3N-LDD were investigated using X-ray photoelectron spectroscopy (XPS) (Figures S7 and S8, Supporting Information). The peaks centered at 932.4 and 952.3 eV in the Cu XPS spectrum reflect the binding energies of $2p_{3/2}$ and $2p_{1/2}$ electrons of Cu(I). In the range of 940–950 eV, no Cu(II) peaks are found. The peak at 397.4 eV can be attributed to N 1s, which indicates the presence of nitrogen in the Cu_3N-LDD particulates and which is in agreement with the results from EDS. In addition, highly crystalline Cu_3N nanocubes (henceforth referred to as Cu_3N-NC) were synthesized through a solution-phase method. Detailed analysis using TEM and HAADF-STEM show that the nanocubes exhibit a uniform shape and narrow size distribution (Figure S9, Supporting Information). The resolved lattice fringes in the HAADF-STEM image correspond with an interplanar spacing of 3.8 Å, matching that of the (100) Bragg reflection of cubic Cu_3N.

After solution synthesis of Cu_3N-HDD, the Cu catalyst derived from it (henceforth referred to as Cu-HDD) was produced in situ by electroreduction of the parent material during CORR (**Figure 2**a). The catalyst particles obtained after different reduction times at −0.65 V versus RHE were deposited on a carbon cloth and subjected to ex situ X-ray diffraction (XRD) measurements. Corresponding results are shown in Figure 2b, verifying a phase transition from space group $Pm\overline{3}m$ to $Fm\overline{3}m$ during reduction. Similar phase transitions are observed during electroreduction of Cu_3N-LDD and Cu_3N-NC to produce Cu-LDD and Cu-NC, respectively (Figures S10 and S11, Supporting Information). To characterize the real-time Cu valence states during electroreduction, operando X-ray absorption (XAS) spectra were recorded at the Cu K-edge (Figure 2c,d). Corresponding spectra recorded during CORR of Cu_3N-HDD at −0.55, −0.65 and −0.75 V versus RHE in the flow cell electrolyzer used for XAS measurements (see Figures S12–S14, Supporting Information) are shown in Figure 2c. The X-ray absorption near-edge structure (XANES) spectra indicate that the Cu valence state change from Cu(I) to Cu(0) during electroreduction, in agreement with the results from ex situ XRD measurements. These findings are further corroborated by the Fourier transforms of the k^3-weighted $\chi(k)$ function of the extended X-ray absorption fine structure (EXAFS) spectra (Figure 2d), showing the disappearance of dominant peak at 1.48 Å for the first coordination shell of Cu—N, and the formation of Cu—Cu coordination at 2.24 Å during CORR.

In order to elucidate the structure-property relationships, the crystalline structures of the different catalysts formed in situ during CORR were investigated. **Figure 3**a–c show the morphologies of the obtained Cu catalysts. HR-TEM images of the

ADVANCED
SCIENCE NEWS
www.advancedsciencenews.com

ADVANCED
MATERIALS
www.advmat.de
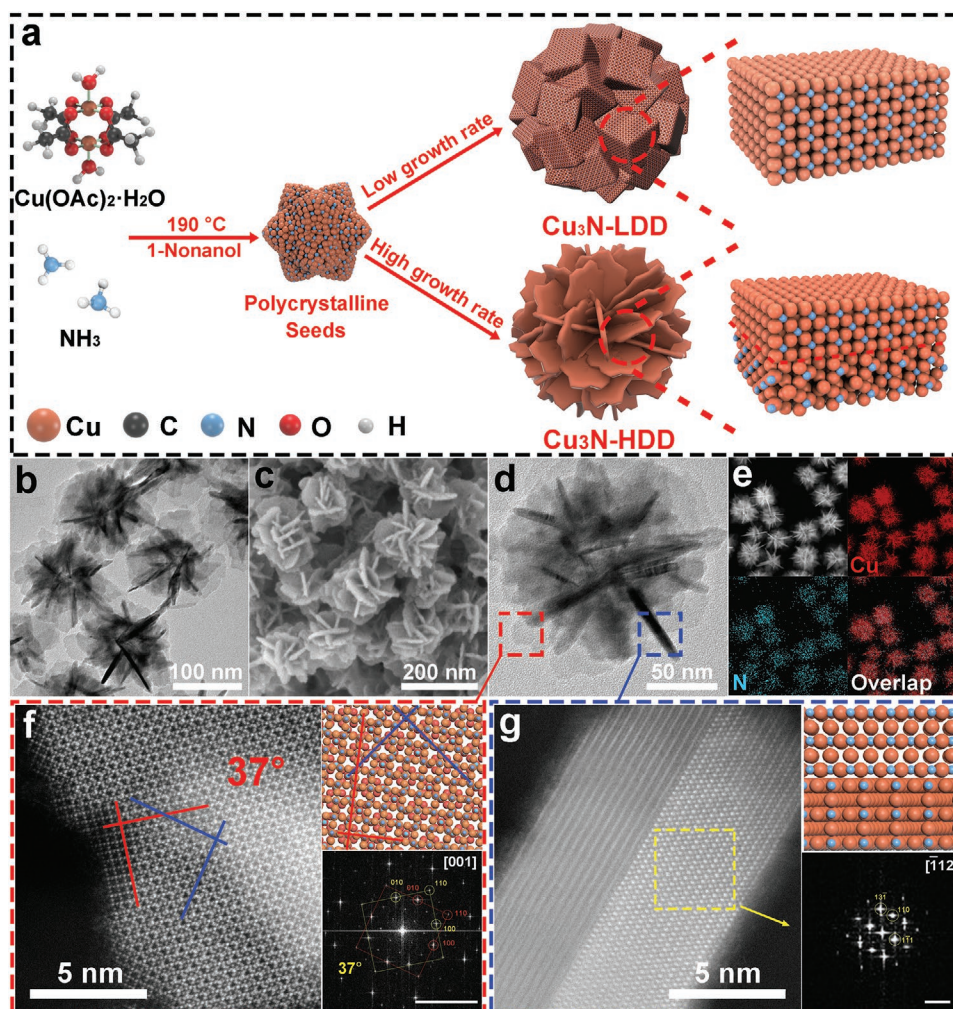
Figure 1. Formation and characterization of Cu₃N-HDD and Cu₃N-LDD nanoparticles. a) Schematic illustration of the synthesis of Cu₃N-HDD and Cu₃N-LDD nanoparticles. b–e) The TEM, SEM, magnified TEM, and corresponding EDS mapping images. The blue and red dashed boxes refer to the differently oriented nanosheets in Cu₃N-HDD. Corresponding HAADF-STEM images are shown in (f) and (g), respectively. The insets in (f) give the schematic structure (top view) and the fast Fourier transform of the HAADF-STEM image, showing a twin structure with a misorientation angle of 37°. The insets in (g) give the schematic structure (side view) and the fast Fourier transform of the HAADF-STEM image, showing a twin structure. The scale bars are $5\,nm^{-1}$.

catalysts are shown in Figure 3d–i. The Cu-HDD and Cu-LDD catalysts consist of nano-sized primary particles of approximate dimensions of 5 and 10 nm, respectively (see Figure 3d–g). The Cu₃N nanocubes change to spherical particles with a diameter of about 65 nm after electroreduction to produce the Cu−NC catalyst (Figure 3h,i). The crystalline structures of the Cu catalysts obtained after CORR were studied using STEM. The surfaces of nanoparticles of Cu-HDD and Cu-LDD consist of a mixture of (100) and (111) facets. The corresponding areas are delineated in Figure 3j,k and Figures S15–S22, Supporting Information with blue and red dashed lines, respectively. The Cu-HDD nanoparticles contain many lattice dislocations with three types of interfaces, namely between (100) and (100), (100) and (111), and (111) and (111). Similar dislocations are found in Cu-LDD, albeit that the density of dislocations is significantly lower than that found in Cu-HDD. Typical fast Fourier transforms of the STEM images of (100) and (111) facets on each

catalyst are shown in Figure 3m–q. The Cu-NC catalyst particles are characterized by a high crystallinity and all facets are of type (100) (Figure 3l,r). Hence, all three Cu catalysts have inherited the crystallinity of their parent Cu₃N structure, that is, the reduction reaction and concomitant release of nitrogen is a topotactic transformation. As discussed below, the different density of dislocations in the catalysts brings about completely different activity in CORR.

The CO electroreduction was performed in a gas-tight flow-cell, fabricated with a CO gas chamber and two electrolyte chambers. To overcome the low solubility of CO in aqueous electrolytes,[4] gas diffusion electrodes (GDEs) were positioned between the gas and electrolyte chambers. The GDEs further provide a large number of three-phase boundaries at the electrode-electrolyte interface and accelerate mass-transport of gaseous reactants and products.[11,19] Gaseous products leave the electrolysis cell with the retentate CO gas stream. The catholyte

ADVANCED
SCIENCE NEWS
www.advancedsciencenews.com

ADVANCED
**MATERIALS**
www.advmat.de
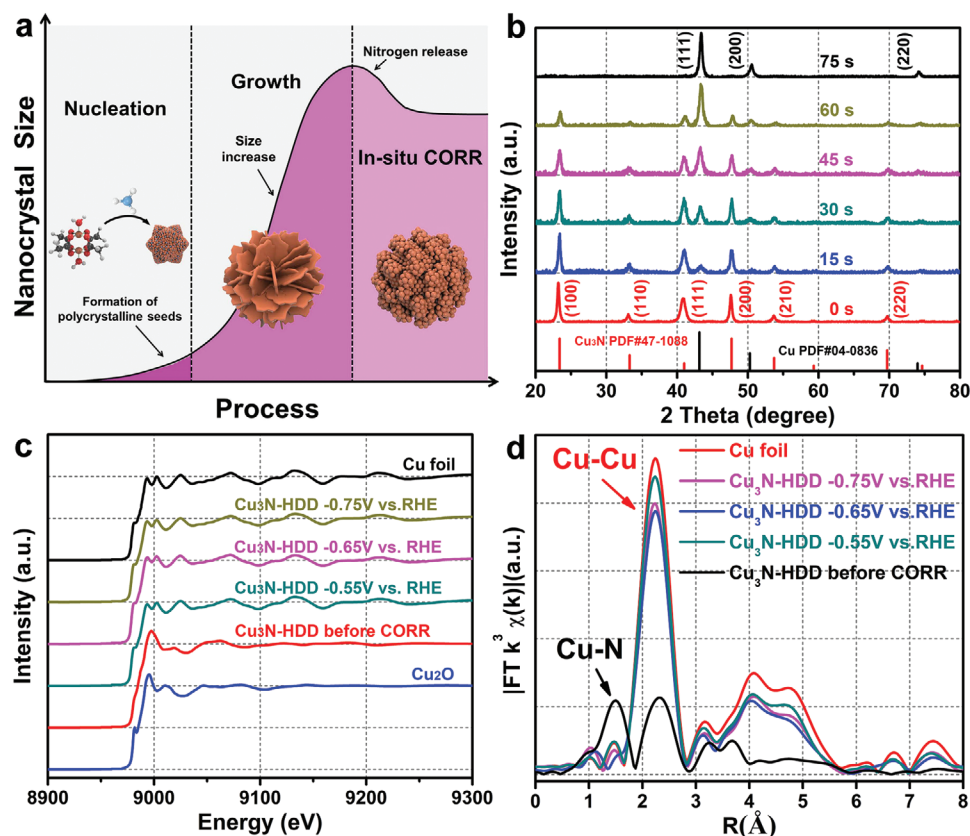
Figure 2. Formation process and analysis of Cu catalyst particles. a) Schematic illustration showing nucleation, growth and in situ formation of the Cu catalyst via electroreduction of Cu_3N during CORR. b) Ex situ XRD patterns of Cu_3N-HDD after different CO electroreduction times at −0.65 V versus RHE in 1.0 M KOH. c) In situ operando Cu K-edge X-ray absorption near-edge structure (XANES) spectra of Cu_3N-HDD in a flow cell electrolyzer at different applied potentials. d) k^3-weighted χ (k) function of the extended X-ray absorption fine structure (EXAFS) spectra.

and anolyte were separated by an anion exchange membrane to avoid the oxidation of generated products. An Ag/AgCl reference electrode was placed in the catholyte. Gaseous products were analyzed by on-line gas chromatography (GC) and liquid products were analyzed by ^1H NMR spectroscopy using DMSO as an internal standard (Table S1, Supporting Information). The CORR activities of Cu-HDD, Cu-LDD, and Cu-NC catalysts found in this study are displayed in **Figure 4**a–c and Figures S23–S26, Supporting Information. Current densities at different applied potentials were measured in 1.0 M KOH solution (Figure 4a). The Cu-HDD catalyst shows a combined C_{2+} Faradaic efficiency of over 90% in the potential range −0.71–0.77 V versus RHE and reaches a total current density up to 1 A cm^{-2} with a C_{2+} Faradaic efficiency of over 80% (Figure 4b). The C_{2+} current normalized to electrochemical surface area (ECSA; Figure S27, Supporting Information) of Cu-HDD is about seven times larger than that of Cu-LDD and more than 13 times than that of Cu-NC at −0.795V versus RHE (Figure 4c), which lends further support to the conclusion that the high activity of Cu-HDD in CO reduction is linked to the high density of lattice dislocations found in this material. A short-term durability test of the Cu-HDD catalyst in CORR was performed using a two-electrode flow-cell configuration. Control experiments were confirmed to exclude the interference of possible impurities (Figure S28, Supporting Information). The measurement was

carried out at a constant current density of 500 mA cm^{-2} in 1.0 M KOH during 300 min. The results show a constant C_{2+} Faradaic efficiency of about 90%, albeit with a slight increase in the cell voltage over time (Figure S29, Supporting Information).

In the flow cell system, a highly alkalic electrolyte (1 M KOH) was used to enhance ionic conductivity and to suppress the competing hydrogen evolution reaction to favor C−C coupling in the electrochemical CO reduction.[11] However, many literature studies have reported a poor long-term performance due to loss of hydrophobicity of the GDEs under alkalic conditions.[1,5,11,20] For this reason, additional experiments were carried out using a catholyte-free MEA system. In the latter configuration, the AEM is sandwiched between the cathodic GDE and the anodic IrO_2-Ti mesh to separate cathode and anode compartments in the cell with serpentine flow channels (Figures S30 and S31, Supporting Information). The minimal gap between the cathode and anode significantly reduces ohmic losses compared with those in a flow cell system.[21] Contrary to the flow cell system, the catholyte-free MEA electrolyzer can be used with a neutral solution as anolyte, maintaining high C_{2+} product selectivities owing to the use of an anion exchange membrane (AEM) that generates a high local pH at the catalyst layer under CO/CO_2RR conditions.[20] The catholyte-free MEA system can even be operated with pure water as anolyte. Corresponding results are shown in Figure 4d, confirming that high
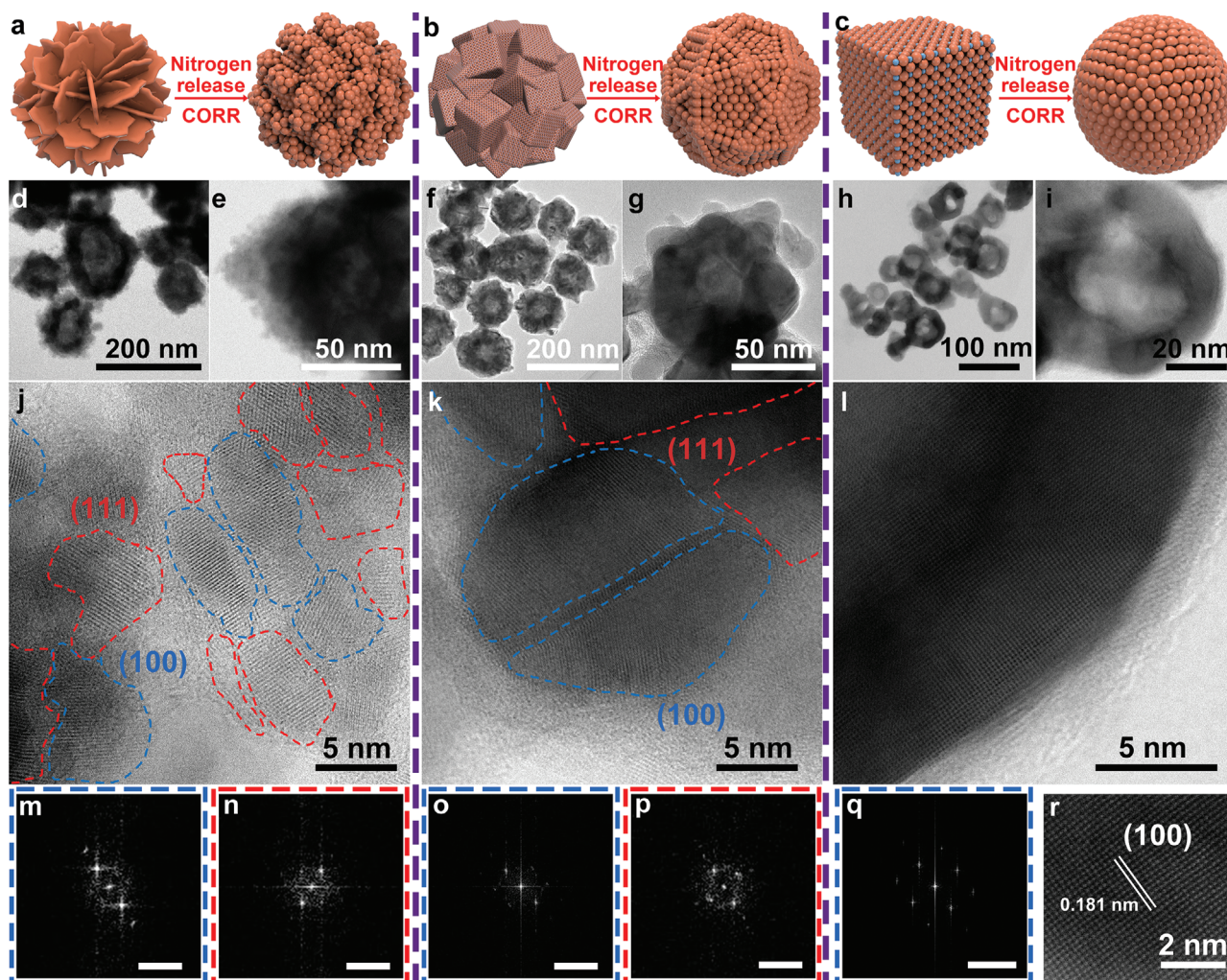
Figure 3. Formation and structural characterization of different Cu catalysts formed in situ during CORR. a–c) Schematic illustration of the electro-reduction of Cu$_3$N-HDD (a) and Cu$_3$N-LDD (b) and Cu$_3$N-NC (c) to Cu during CORR. d,f,h) TEM, e,g,i) magnified TEM images, and j–l) STEM images of the Cu catalysts obtained during CORR: d,e,j) Cu-HDD, f,g,k) Cu-LDD, and h,i,l) Cu-NC. The areas delineated by blue and red dashed lines in (j) and (k) denote the (100) and (111) facets, respectively. m–p) The corresponding fast Fourier transforms of the Cu(100) and Cu(111) STEM images, while (q) shows the fast Fourier transforms image of STEM image of Cu derived from Cu-NC. The scale bars are 10 nm^{-1}. r) HAADF-STEM image of Cu-NC.

currents and excellent C$_{2+}$ product selectivities can be obtained under these conditions. The measurements showed a negligible production of methane and methanol with a combined Faradic efficiency of less than 0.5% over all assessed voltages, while acetate was detected only in the anolyte (Figures S32–S34, Supporting Information). Furthermore, the IrO$_2$-Ti mesh anode shows minimal activity for acetate and alcohol oxidation, which was confirmed in a control experiment in which the cell was operated at 1.0 A cell current under HER conditions, that is, without supply of CO (Figure S35, Supporting Information). The durability of the catholyte-free MEA system in CORR significantly outperformed that of the flow cell electrolyzer, which is probably due to flooding of the high concentration electrolyte used in the flow cell system, preventing diffusion of CO and gas products through the GDE.[20,21] The constructed MEA system showed a stable cell voltage of 3.94 V with a C$_{2+}$ product selectivity of over 90% during continuous operation for 20 h at 1.0 A cell current (Figure S36, Supporting Information), and

delivered a gaseous product stream with 19.7 vol% ethylene and a liquid stream with concentrations 1.06 M ethanol and 0.45 M n-propanol at the outlet of the cathode (Table S2, Supporting Information). Because most liquid products cross the AEM to the anolyte by diffusion and electroosmotic drag,[20] the catholyte-free MEA system cannot produce a highly concentrated liquid product stream.

Attempting to obtain both high-concentration gas and liquid streams, we also investigated a catholyte-free MEA system adapted with a porous cation exchange resin as a solid-state electrolyte to enhance proton transport (henceforth referred to as MEA-SSE). In this configuration (Figures S37 and S38, Supporting Information), the generated liquid products that cross the AEM are carried away by the deionized water stream. H$_2$ gas was used as a feedstock at the anode compartment to promote electrocatalytic hydrogenation of CO and to avoid O$_2$ as byproduct. Its use is further motivated by the fact that the hydrogen oxidation reaction proceeds at a lower
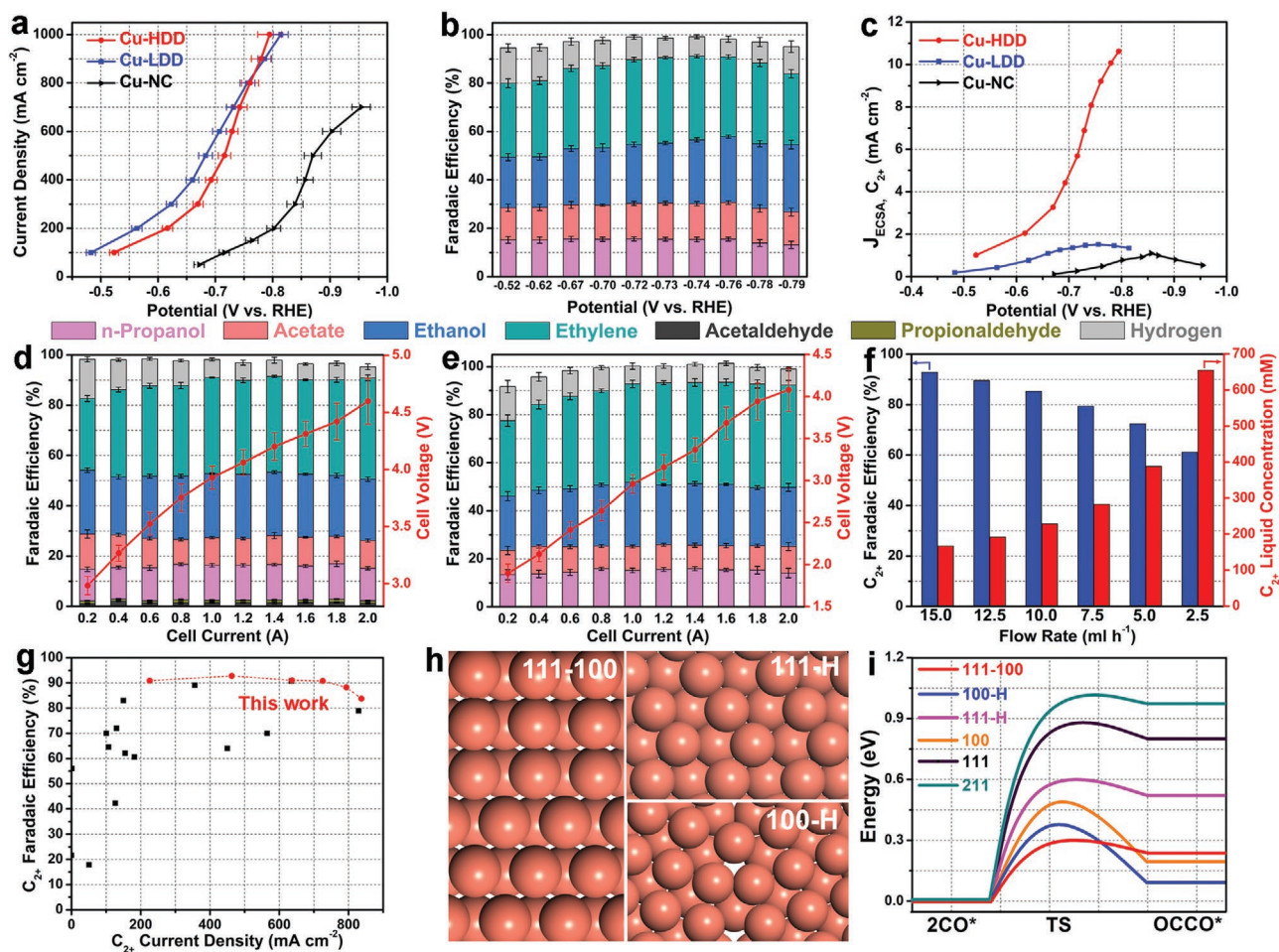
Figure 4. Performance of Cu-HDD, Cu-LDD, and Cu-NC catalysts in CORR using different electrolyzer cell configurations and results of first-principles calculations. a–c) Flow cell electrolyzer: a) current density for CO reduction as a function of applied potential, b) Faradaic efficiency for CO reduction products at different potentials for Cu-HDD, and c) C_{2+} current densities (normalized to the ECSA) as a function of applied potential. d,e) Faradaic efficiency for CO electroreduction and cell voltage at different cell currents in the catholyte-free MEA (d) and MEA-SSE (e) electrolyzers. f) C_{2+} liquid concentration and corresponding C_{2+} Faradaic efficiency as a function of the deionized water flow rate. Error bars represent the standard deviation from at least three independent measurements. g) Comparison of C_{2+} Faradaic efficiencies at different C_{2+} current densities for Cu-HDD with state-of-the-art CORR electrodes reported in literature.[1–3,7,9,18] (For further details, see Table S4, Supporting Information). h) Top view of the atomic structure of three possible interfaces between Cu(111) and Cu(100) facets (labeled 111-H, 100-H, and 111-100; see main text). i) Energy diagrams of CO* dimerization on different Cu interfaces and facets.

over potential than the oxygen evolution reaction, which may decrease the cell voltage and increase the energy efficiency. As shown in Figure 4e, the MEA-SSE system can not only deliver superb CORR activities, but also delivers a high concentration of C_{2+} liquid products up to a concentration of 655×10^{-3} M at the outlet of the solid state electrolyte-containment layer upon decreasing the flow rate of the deionized water stream to 2.5 mL h^{-1} (Figure 4f and Figures S39 and S40, Supporting Information). The durability of the MEA-SSE electrolyzer was evaluated at a constant cell current of 1.0 A. A continuous C_{2+} production was achieved over the duration (20 h) of the electrolysis experiment, involving a gas stream with 17.4 vol% of ethylene and a liquid stream with a total concentration of 1.45 M C_{2+} products (ethanol and n-propanol) at the outlet of the cathode, and a liquid stream with a total concentration of 230×10^{-3} M C_{2+} products (ethanol, acetic acid, n-propanol) at the exit port of the SSE-containment layer. (Figure S41 and

Table S3, Supporting Information). In terms of both C_{2+} partial current density and C_{2+} Faradaic efficiency, the Cu-HDD catalyst outperforms most state-of-the-art CORR electrocatalysts as is shown in Figure 4g.

As found in this study, also other studies have demonstrated that the obtained C_2 yields show a pH dependence on the RHE scale,[22] indicating that non proton-coupled electron transfer reaction is the rate-determining step in the C_2 formation mechanism. Many theoretical studies have proposed that the formation of a CO* dimer dominates the C−C coupling reaction on the Cu surface.[23] For this reason DFT calculations were carried out to examine the role of crystal facets and the presence of dislocations on CO* dimerization on Cu-HDD in CORR. Structural characterization carried out in this work has demonstrated that the surfaces of Cu-HDD nanoparticles are mainly composed of (111) and (100) facets (Figures 2b,3 and Figures S15–S18, Supporting Information). It may therefore be

**ADVANCED
SCIENCE NEWS**

www.advancedsciencenews.com

**ADVANCED
MATERIALS**

www.advmat.de

assumed that either one or two, or all three interfaces between these facets, labeled 111-H (Σ3{111}), 100-H (Σ5{100}), and 111-100 as shown in Figure 4h, are responsible to selective formation of C_2 products. The computed coupling energy profiles and optimized adsorbate configurations for different surfaces and facets are shown in Figure 4i and Figures S42 and S43, Supporting Information, respectively. In agreement with the C_1-C_2 selectivities reported in ref. [3], we find that CO* dimerization is more favored on (100) than on (111) and (211) facets. The calculations further reveal that, in particular, dislocations 111-100 and 100-H significantly reduce the energy barrier toward CO* dimerization (Figure 4i).

In conclusion, we successfully prepared copper nitride (Cu_3N) nanocrystals with a controlled density of twin structures through regulating the kinetics of crystal growth. The $Cu°$ electrocatalysts obtained by in situ reduction of Cu_3N and concomitant release of nitrogen during CORR inherit the defective crystallinity of their parent structures during the topotactic transformation, that is, with a controlled density of lattice dislocations. In general, this work will guide the design and preparation of high-performance catalysts based on metal nanoparticles. Not only we have demonstrated that implementation of an electrocatalyst based upon $Cu°$ nanoparticles with a high density of dislocations in a catholyte-free MEA system for CO reduction delivers industrial-scale currents and superb selectivities toward C_{2+} products, but also that such an MEA electrolyzer can be operated with pure deionized water as the anolyte. The use of non-corrosive water will increase operational life and reliability of the MEA electrolyzers. When the catholyte-free MEA electrolyzer is further adapted with a porous cation exchange resin as solid-state electrolyte to maximize production, high concentration gas and liquid C_{2+} streams are obtained, advancing toward the ultimate goal of commercially viable CO electrolyzers.

Experimental Section

Chemicals: Analytical grade hexane, ethanol, chloroform, copper (II) nitrate trihydrate, copper (I) acetate monohydrate, and potassium hydroxide (KOH) were obtained from Sinopharm Chemical Reagents, China. Nafion solution (5%), 1-octadecylamine ($\geq$99%), and oleylamine (70%) were purchased from Aldrich. 1-Nonanol ($\geq$98%) was purchased from Aladdin. Iridium(III) chloride hydrate ($IrCl_3 \cdot xH_2O$, 99.9%) was purchased from Alfa Aesar. All of the chemicals used in this experiment were analytical grade and used without further purification. Deionized (DI) water from a Milli-Q System (Millipore, Billerica, MA, USA) was used in all experiments.

Synthesis of Cu_3N with a High Density of Lattice Dislocations: In a typical procedure, 200 mg copper(II) acetate monohydrate was added to 100 mL 1-nonanol. The liquid dispersion was bubbled with ammonia at room temperature under vigorously stirring until the copper(II) acetate monohydrate was dissolved completely. The obtained solution was degassed at 110 °C for 1 h under a flow of ammonia. Next, the solution was heated at 190 °C in an oil bath for 30 min (heating rate 5 °C min^{-1}) in a stream of ammonia (300 mL min^{-1}, ammonia was bubbled into the liquid solution). During heating, the color of the deep blue solution suddenly changed to brown at 185 °C. After the product was naturally cooled down to room temperature, it was centrifuged and washed with hexane three times and dried in vacuum at room temperature overnight.

Synthesis of Cu_3N with a Low Density of Lattice Dislocations: The synthesis of Cu_3N-LDD was analogous to that of Cu_3N-HDD, with the difference that the ammonia flow rate was set at 30 mL min^{-1} (ammonia was bubbled into the liquid solution) during heating of the solution at 190 °C for 30 min.

Synthesis of Cu_3N Nanocubes: 100 mg of copper (II) nitrate trihydrate was dissolved in a mixture of 2.5 g 1-octadecylamine (ODA) and 6 mmol of oleylamine (OAm). The obtained solution was degassed using a flow of nitrogen at 110 °C for 1 h. The obtained solution was subsequently heated under nitrogen at 250 °C in an oil bath for 20 min (heating rate 10 °C min^{-1}). The obtained black-brown mixture was naturally cooled to 60 °C. Next, 40 mL ethanol was added to the solution and the precipitate was collected by centrifugation at 8000 rpm. The product was washed several times with hexane, ethanol, and chloroform and subsequently redispersed in hexane.

Supporting Information

Supporting Information is available from the Wiley Online Library or from the author.

Conflict of Interest

The authors declare no conflict of interest.

Keywords

[1] M. Jouny, W. Luc, F. Jiao, *Nat. Catal.* **2018**, *1*, 748.

[2] T.-T. Zhuang, Y. Pang, Z.-Q. Liang, Z. Wang, Y. Li, C.-S. Tan, J. Li, C. T. Dinh, P. De Luna, P.-L. Hsieh, *Nat. Catal.* **2018**, *1*, 946.

[3] Y. Pang, J. Li, Z. Wang, C.-S. Tan, P.-L. Hsieh, T.-T. Zhuang, Z.-Q. Liang, C. Zou, X. Wang, P. De Luna, *Nat. Catal.* **2019**, *2*, 251.

[4] C. Chen, J. F. K. Kotyk, S. W. Sheehan, *Chem* **2018**, *4*, 2571.

[5] C. Xia, P. Zhu, Q. Jiang, Y. Pan, W. Liang, E. Stavitsk, H. N. Alshareef, H. Wang, *Nat. Energy* **2019**, *4*, 776.

[6] a) S. Ren, D. Joulié, D. Salvatore, K. Torbensen, M. Wang, M. Robert, C. P. Berlinguette, *Science* **2019**, *365*, 367; b) T. Möller, W. Ju, A. Bagger, X. Wang, F. Luo, T. N. Thanh, A. S. Varela, J. Rossmeisl, P. Strasser, *Energy Environ. Sci.* **2019**, *12*, 640; c) C. Zhao, Y. Wang, Z. Li, W. Chen, Q. Xu, D. He, D. Xi, Q. Zhang,

**ADVANCED
SCIENCE NEWS**

www.advancedsciencenews.com

**ADVANCED
MATERIALS**

www.advmat.de

T. Yuan, Y. Qu, *Joule* **2019**, *3*, 584; d) T. Zheng, K. Jiang, N. Ta, Y. Hu, J. Zeng, J. Liu, H. Wang, *Joule* **2019**, *3*, 265. e) N. Corbin, J. Zeng, K. Williams, K. Manthiram, *Nano Res.* **2019**, *12*, 2093.

[7] D. S. Ripatti, T. R. Veltman, M. W. Kanan, *Joule* **2019**, *3*, 240.

[8] X. Wang, J. F. de Araújo, W. Ju, A. Bagger, H. Schmies, S. Kühl, J. Rossmeisl, P. Strasser, *Nat. Nanotech.* **2019**, *14*, 1063.

[9] J. Li, F. Che, Y. Pang, C. Zou, J. Y. Howe, T. Burdyny, J. P. Edwards, Y. Wang, F. Li, Z. Wang, *Nat. Commun.* **2018**, *9*, 4614.

[10] a) S. Nitopi, E. Bertheussen, S. B. Scott, X. Liu, A. K. Engstfeld, S. Horch, B. Seger, I. E. Stephens, K. Chan, C. Hahn, *Chem. Rev.* **2019**, *119*, 7610; b) D. Tan, J. Zhang, L. Yao, X. Tan, X. Cheng, Q. Wan, B. Han, L. Zheng, J. Zhang, *Nano Res.* **2020**, *13*, 768.

[11] C.-T. Dinh, T. Burdyny, M. G. Kibria, A. Seifitokaldani, C. M. Gabardo, F. P. García de Arquer, A. Kiani, J. P. Edwards, P. De Luna, O. S. Bushuyev, *Science* **2018**, *360*, 783.

[12] a) Y. Wang, P. Han, X. Lv, L. Zhang, G. Zheng, *Joule* **2018**, *2*, 2551; b) C. W. Li, J. Ciston, M. W. Kanan, *Nature* **2014**, *508*, 504; b) X. Feng, K. Jiang, S. Fan, M. W. Kanan, *J. Am. Chem. Soc.* **2015**, *137*, 4606; c) X. Feng, K. Jiang, S. Fan, M. W. Kanan, *ACS Cent. Sci.* **2016**, *2*, 169.

[13] X. Zhang, X. Sun, S.-X. Guo, A. M. Bond, J. Zhang, *Energy Environ. Sci.* **2019**, *12*, 1334.

[14] R. Reske, H. Mistry, F. Behafarid, B. Roldan Cuenya, P. Strasser, *J. Am. Chem. Soc.* **2014**, *136*, 6978.

[15] Y. Wang, H.-C. Peng, J. Liu, C. Z. Huang, Y. Xia, *Nano Lett.* **2015**, *15*, 1445.

[16] a) H. Zheng, R. K. Smith, Y.-W. Jun, C. Kisielowski, U. Dahmen, A. P. Alivisatos, *Science* **2009**, *324*, 1309; b) B. Lim, H. Kobayashi, P. H. Camargo, L. F. Allard, J. Liu, Y. Xia, *Nano Res.* **2010**, *3*, 180.

[17] Y. Yin, A. P. Alivisatos, *Nature* **2005**, *437*, 664.

[18] a) W. Luc, X. Fu, J. Shi, J.-J. Lv, M. Jouny, B. H. Ko, Y. Xu, Q. Tu, X. Hu, J. Wu, *Nat. Catal.* **2019**, *2*, 423; b) D. Raciti, L. Cao, K. J. Livi, P. F. Rottmann, X. Tang, C. Li, Z. Hicks, K. H. Bowen, K. J. Hemker, T. Mueller, *ACS Catal.* **2017**, *7*, 4467; c) J. Li, K. Chang, H. Zhang, M. He, W. A. Goddard, J. G. Chen, M.-J. Cheng, Q. Lu, *ACS Catal.* **2019**, *9*, 4709; d) L. Han, W. Zhou, C. Xiang, *ACS Energy Lett.* **2018**, *3*, 855; e) E. Bertheussen, T. V. Hogg, Y. Abghoui, A. K. Engstfeld, I. Chorkendorff, I. E. Stephens, *ACS Energy Lett.* **2018**, *3*, 634.

[19] M. G. Kibria, J. P. Edwards, C. M. Gabardo, C. T. Dinh, A. Seifitokaldani, D. Sinton, E. H. Sargent, *Adv. Mater.* **2019**, *31*, 1807166.

[20] C. M. Gabardo, C. P. O'Brien, J. P. Edwards, C. McCallum, Y. Xu, C.-T. Dinh, J. Li, E. H. Sargent, D. Sinton, *Joule* **2019**, *3*, 2777.

[21] Z. Yin, H. Peng, X. Wei, H. Zhou, J. Gong, M. Huai, X. Li, G. Wang, J. Lu, L. Zhuang, *Energy Environ. Sci.* **2019**, *12*, 2455.

[22] a) Y. I. Hori, *Modern Aspects of Electrochemistry*, Springer, New York **2008**, pp. 89; b) K. J. P. Schouten, E. Pérez Gallent, M. T. Koper, *ACS Catal.* **2013**, *3*, 1292.

[23] a) K. Schouten, Y. Kwon, C. Van der Ham, Z. Qin, M. Koper, *Chem. Sci.* **2011**, *2*, 1902; b) J. H. Montoya, C. Shi, K. Chan, J. K. Nørskov, *J. Phys. Chem. Lett.* **2015**, *6*, 2032.

2002382 (8 of 8)